Published in final edited form as:
J Magn Reson. 2014 September ; 246: 36–45. doi:10.1016/j.jmr.2014.06.017.

Nonparametric pore size distribution using d-PFG: Comparison to s-PFG and migration to MRI

Dan Benjamini[a,b], **Michal E. Komlosh**[a,c], **Peter J. Basser**[a], **Uri Nevo**[b,*]

[a]Section on Tissue Biophysics and Biomimetics, PPITS, Eunice Kennedy Shriver, National Institute of Child Health and Human Development, NIH, Bethesda, MD, USA

[b]Department of Biomedical Engineering, The Iby and Aladar Fleischman Faculty of Engineering, Tel-Aviv University, Tel-Aviv, Israel

[c]Center for Neuroscience and Regenerative Medicine, Uniform Service University of the Health Sciences, Bethesda, MD, USA

Abstract

Here we present the successful translation of a pore size distribution (PSD) estimation method from NMR to MRI. This approach is validated using a well-characterized MRI phantom consisting of stacked glass capillary arrays (GCA) having different diameters. By employing a double pulsed-field gradient (d-PFG) MRI sequence, this method overcomes several important theoretical and experimental limitations of previous single-PFG (s-PFG) based MRI methods by allowing the relative diffusion gradients' direction to vary. This feature adds an essential second dimension in the parameters space, which can potentially improve the reliability and stability of the PSD estimation. To infer PSDs from the MRI data in each voxel an inverse linear problem is solved in conjunction with the multiple correlation function (MCF) framework, which can account for arbitrary experimental parameters (e.g., long diffusion pulses). This scheme makes no *a priori* assumptions about the functional form of the underlying PSD. Creative use of region of interest (ROI) analysis allows us to create different underlying PSDs using the same GCA MRI phantom. We show that an s-PFG experiment on the GCA phantom fails to accurately reconstruct the size distribution, thus demonstrating the superiority of the d-PFG experiment. In addition, signal simulations corrupted by different noise levels were used to generate continuous and complex PSDs, which were then successfully reconstructed. Finally, owing to the reduced *q*- or *b*-values required to measure microscopic PSDs via d-PFG MRI, this method will be better suited to biomedical and clinical applications, in which gradient strength of scanners is limited.

Keywords

MRI; Double pulsed field gradient; Pore size distribution; NMR; Nonparametric; Empirical

---

[*]Corresponding author. nevouri@eng.tau.ac.il (U. Nevo).

1. Introduction

Noninvasive characterization of porous media is critical to many scientific and technical fields, including material sciences [1,2], food sciences [3], well-logging [4], biotechnology, and medicine [5]. In biological tissue, and specifically nerve tissue, it is useful to treat axons as porous media—water-filled infinite cylindrical “pores.” The microstructure of this porous media can provide useful information about whether the tissue is normal, diseased, or degenerated, and in the case of unmyelinated and myelinated axons, the information that can be transmitted along them, since their conduction velocity scales with axon size [6,7]. Moreover, several diseases, such as amyotrophic lateral sclerosis and multiple sclerosis, have been known to alter the axon size distribution [8,9].

The mean axonal pore size is an important parameter that may help determine functional properties of nerves, and diffusion-weighted MR is an efficient way to obtain such information. A single pulsed-field gradient (s-PFG) experiment [10] is most commonly used to encode the spins’ net displacement, and the average dimension of the medium can be inferred from the resulting signal attenuation [11]. In cases where the expected variance in pore size is low, this technique has been used to characterize narrowly distributed emulsions [12], red blood cells [13], and packed monodisperse polystyrene spheres [14]. A recently proposed approach further expands the capabilities of the s-PFG experiment by using a modified Stejskal-Tanner sequence that preserves the phase information, thus revealing the pore space function [15]. However, due to the inverse relationship between the pore diameter and the scattering vector magnitude, $\mathbf{q} \equiv (2\boldsymbol{\pi})^{-1}\gamma\delta\mathbf{G}$ ($\mathbf{G}$ is the gradient wave vector and its duration δ, and $\boldsymbol{\gamma}$ is the gyromagnetic ratio), obtaining fine microstructure detail requires a large q-value ($q = |\mathbf{q}|$). Such gradients are an order of magnitude stronger than what is currently available on conventional clinical scanners, making such measurements infeasible [16].

In addition to biological samples, diffusion weighted NMR can be useful for characterizing porous biomaterials, since their porosity dictates the release rate of drugs or other bioactive agents from them [1], and affects their biocompatibility [17] and longevity [18]. Following implantation, some of these materials undergo structural changes in the body, which can be tracked *in vivo* using the NMR- and MRI-based methods.

An expansion of the s-PFG, the double-PFG (d-PFG) experiment [19,20], includes two PFG pairs that are applied successively, separated by a mixing time, $\boldsymbol{\tau}_m$. With long $\boldsymbol{\tau}_m$, this method is sensitive to microscopic [21] and compartment shape [20,22,23] anisotropy, while for vanishing $\boldsymbol{\tau}_m$ the pore dimensions can be obtained [5,24–26]. In addition, the relative angle between the successive PFG blocks, φ, can be varied; thus the d-PFG experiment adds a second dimension in space of pulse timing parameters.

While knowledge of the average pore size is valuable, it is preferable to determine the entire pore size distribution (PSD) of the sample. From it, one can infer the mean pore size or first moment, but also all other higher moments, which can provide additional information about the pore morphology and microstructure. Parametric PSD estimation of white matter tissue was previously demonstrated using data from an s-PFG experiment with varying diffusion periods [27], while assuming a γ-distribution for the PSD. Obtaining the PSD using a nonparametric distribution (i.e., one with no *a priori* assumption about the parametric form of the distribution) would provide comprehensive subvoxel micro-structural information without introducing this bias. Estimation of such an empirical pore size distribution has been previously demonstrated with s-PFG NMR in conjunction with solving an inverse linear problem [2]. In this case the solution depends on the degree of linear independence (degree of correlation between the different independent variables [28]) of the matrix that describes the set of linear equations. As the degree of multicollinearity rises, the solution becomes more ill-conditioned.

Recently, this linear approach was extended to include a second dimension in the parameter space by using a d-PFG experiment [29]. The 2-D method was shown to reduce multicollinearity and thus improve the stability and reliability of the estimated empirical PSD [29,30]. Moreover, this 2-D NMR method was validated after being used on calibrated microcapillary PSD phantoms, resulting in accurate size distribution estimation [31]. To account for a continuous size distribution, this NMR technique was subsequently applied on porous bioresorbable polymer films, which are designed to release drugs in a controlled fashion [32]. The reliability of the estimations was confirmed upon comparison to scanning electron microscopy based analysis, which is the conventional characterization method of bioresorbable polymers.

Here we present the successful translation of this 2-D method from NMR to MRI, and demonstrate the faithful estimation of a known PSD along with different free water fractions using a well-characterized MRI size distribution phantom. We then show how the addition of the second gradient pair significantly improves the estimation. Finally, we examine by simulations the estimation quality of complex and continuous PSDs under different noise levels.

2. Theory

For many purposes, porous specimen can be modeled as comprising two components (according to the type of diffusion water molecules experience within them); one is restricted and the other is Gaussian (free diffusion). Using this bi-compartmental model in biological applications is common [33]. In packs of axons, the restricted component is usually said to be the intra-cellular content, while water in the extra-cellular space is assumed to experience free diffusion. If monodispersity is not assumed (i.e., the PSD is not a delta function), the MR signal in the restricted diffusion component is a superposition of signals from a distribution of different pore sizes [34]. Depending on the type of sample, the pores can be selected to be spherical, parallel plates, or cylindrical as in the present study.

Using s-PFG NMR pulse sequences, one measures the signal attenuation at different q-values and then infers the PSD from the measured decay curve. The d-PFG pulse sequence (Fig. 1) introduces another experimental parameter to further constrain this inverse problem. This experiment produces an NMR signal from water molecules restricted in pores of radius R that is expressed as $E_{rest}(G_1, G_2, \varphi, R)$. In the current study, the restricted signal is calculated (for each value of G_1, G_2, φ, and R) using the Multiple Correlation Function

(MCF) method [35,36]. The restricted component is assumed to be composed of N different compartment sizes, R_i. The Gaussian component results in the signal $E_G(G_1, G_2, \varphi)$, which is calculated according to Stejskal and Tanner [10],

$$E_G(\mathbf{G}, \varphi) = exp\left[-\gamma^2 D \int_0^T dt \left| \int_0^t \mathbf{G}(t')dt' \right|^2 \right], \tag{1}$$

where D is the diffusion coefficient, T is the time to echo, and γ is the gyromagnetic ratio. For the d-PFG pulse sequence (Fig. 1) Eq. (1) is reduced to

$$E_G(G_1, G_2, \varphi) = e^{-\gamma^2 D\delta^2\left[\left(\Delta - \frac{\delta}{3}\right)\left(G_1^2 + G_2^2\right) - \left(\frac{\delta}{3}\right)G_1 G_2 cos(\varphi)\right]}. \tag{2}$$

Because the two compartments are not exchanging, the signal from the entire sample is the superposition of the calculated signals from the restricted and Gaussian compartments, and is expressed as

$$E(G_1, G_2, \varphi) = \sum_{i=1}^{N} f_i E_{rest}(G_1, G_2, \varphi, R_i) + f_G E_G(G_1, G_2, \varphi), \tag{3}$$

where f_i are the volumetric fractions that satisfy $\sum_{i=1}^{N} f_i + f_G = 1$. By varying both G and φ in the 2-D parametric space, a linear set of equations is obtained from Eq. (3), which can be written as the matrix equation

$$\mathbf{E} = \mathbb{E}\mathbf{f}, \tag{4}$$

where $\mathbf{E}$ is the experimental data vector, $\mathbf{f}$ is the vector of relative volumetric fractions of each pore radius, and $\mathbb{E}$ is the transfer matrix.

3. Methods

3.1. MRI phantom and hardware

Fig. 2 shows a photograph of the PSD MRI phantom placed inside an NMR tube. The PSD phantom consists of glass capillary arrays (GCA) or wafers [26] whose diameter is close to the inner diameter of the NMR tube. Here we construct our phantom using six parallel packs of water-filled microcapillary wafers (Photonis, Sturbridge, MA), with three distinct pore radii, namely, four with $R = 2.5$ µm tubes, two with $R = 5$ µm tubes, and two with $R = 13.7$ µm tubes. The microcapillary arrays were filled with pure water using a three-step procedure, which is detailed elsewhere [26]. The GCA phantom was placed in a 15 mm NMR tube (New Era Enterprises Inc., Vineland, NJ), and inserted into the magnet's bore with the long axis of the capillaries aligned with the direction of the main magnetic field. All experiments were performed on a 7 T vertical-bore Bruker AVANCE III spectrometer equipped with a micro-2.5 gradient set oriented along its magnetic field (z axis).

In many cases, sub-voxel resolution can provide important new microstructural information. The ability to obtain a PSD from a pixel-by-pixel analysis is therefore a desirable goal to effectively enhance spatial resolution, allowing one to drill down into the voxel. The PSD phantom used in the present study does not allow such an analysis in the in-plane directions since the wafer thickness is larger than the spatial resolution (i.e., each voxel contains a single pore size). For lack of sub-voxel PSD, we turned to ROI-based analysis, which bears the closest resemblance to a pixel-by-pixel analysis. We demonstrate here, by selecting different ROIs and estimating the PSD within them, the versatility of this 2-D method.

We have used the signal intensity from a proton density image to calculate the relative water content of each GCA within a certain ROI. This strategy provides a direct and accurate measurement of the actual volumetric fraction. Relying on the physical characteristics provided by the manufacturer may lead to a errors due to structural imperfections (as indicated in Fig. 3G) and imperfect water-filling of the capillaries.

3.2. Experimental parameters

The d-PFG filtered MRI pulse sequence used in this study is detailed in Fig. 1. The sequence starts with a d-PFG filter that includes application of hard radiofrequency (RF) pulses. Three effective gradient pulses of duration $\delta = \delta_1 = \delta_2$, with a separation period of $\Delta = \Delta_1 = \Delta_2$, provide the diffusion encoding. The magnitude and the direction of the two gradients of the d-PFG encoding are specified by the vectors $\mathbf{G_1}$ and $\mathbf{G_2}$. The three effective gradients can be viewed as two pairs of diffusion gradients with no mixing time between them. The d-PFG encoded magnetization is subsequently fed into a standard imaging sequence with soft RF pulses to enable slice selection.

Double-PFG acquisition parameters were: $\delta = 1.65$ ms, $\Delta = 45$ ms, $t_m = 0$. Eight diffusion gradient magnitudes were used, $G = G_1 = G_2 = 0 - 605$ mT/m, resulting in $q_{max} = 425$ cm^{-1}. The angle φ was varied in the XY plane, which is the plane whose normal vector lies parallel to the axis of the GCAs microcapillaries. Ten different angles were used in the range $\varphi = 0 - \pi$. MRI acquisition parameters were: $TR = 5$ s, $TE = 7.75$ ms, $NA = 1$, $ST = 1.1$ ms, and spatial resolution = $0.242 \times 0.242 \times 1$ mm^3. A total of 80 acquisitions were sufficient to obtain an accurate PSD in each voxel, which resulted in an experimental time of 7 h.

It was already shown, for similar experimental parameters and a long separation time (ST) between the diffusion filter and the imaging block, that the effect of incorporating imaging gradients in the signal calculation is negligible [26]. In addition, it is suggested that if ST is shorter than the characteristic time it takes the spins to sample the pore, imaging gradients should not be ignored. In our case, the separation time was set to the minimum to allow the shortest possible TE, and therefore does not allow full sampling of the largest pore within the system. In addition, the slice orientation in the present study is sagittal, therefore the slice-select gradients are applied in the direction of the diffusion encoding (i.e., perpendicular to the cylinder’s axis). Owing to the MCF framework, the calculated theoretical signal attenuations took into account slice-select and diffusion gradients, along with all other experimental parameters.

When $\varphi = \pi$ the d-PFG is in fact an s-PFG experiment with a diffusion period of 2Δ. Such an s-PFG subset from the acquired d-PFG data was taken and analyzed for performance comparison reasons. To allow a fair study, q_{max} in the s-PFG experiment was kept identical to the one used in the d-PFG experiment. In contrast to the d-PFG, in an s-PFG experiment the relative angle, φ, does not exist, therefore leading to a single-varied experimental parameter, G. To obtain the maximal amount of information, the gradient amplitude was acquired with the smallest increments allowed by the current hardware, and resulted in 42 steps in the same gradient range used in the d-PFG protocol.

3.3. Simulations

Simulations were performed to demonstrate the capabilities of the suggested framework to estimate continuous PSDs with a more complex and realistic shape (other than the discrete PSD of the phantom). Two different PSDs were simulated:

1. A Bimodal-Gaussian PSD with means of $\mu_1 = 6.84$ μm and $\mu_2 = 11.99$ μm, standard deviations of $\sigma_1 = 1.5$ μm and $\sigma_2 = 2.0$ μm, and relative fractions of 0.375 and 0.625.
2. A more complex PSD that is composed of three peaks. The first peak is lognormal with $\mu_1 = 3.00$ μm, and standard deviation of $\sigma_1 = 4.0$ μm. The other two peaks are Gaussian with means of $\mu_2 = 11.65$ μm and $\mu_3 = 16.28$ μm, and standard deviations of $\sigma_2 = 1.1$ μm and $\sigma_3 = 1.2$ μm. The relative fractions are 0.35, 0.4, and 0.25, respectively.

To approach the continuous nature of an actual size distribution, the signal attenuation profile was generated using a transfer matrix with very fine equal-sized spatial increments in R (0.17 μm). In addition, all of the generated signal curves were corrupted by Gaussian white noise. For each distribution, two noise standard deviations were analyzed, namely, 0.5% and 1% relative to the signal attenuation without any diffusion gradient applied.

3.4. PSD estimation

In the current study we assumed $N = 50$ restricted compartments, with radii in the range of 1 − 18 μm, which resulted in a PSD with 0.35 μm bins. All implementations of the theory were performed with *Matlab*® (R2013a, The MathWorks, Natick, MA) in-house algorithms. The partial volumetric fraction vector, **f**, was then obtained by implementing a non-negative least-square algorithm with an added constraint, that $\sum_{i=1}^{N} f_i + f_G = 1$, using the *lsqlin* Matlab function. Note that no regularization was used in the fitting process, since the PSD reconstructions were stable to increased noise level, as shown in the Results.

While in the d-PFG case the transfer matrix is better conditioned than for an s-PFG experiment, the inversion remains ill-conditioned. The important properties of the transfer matrix in the context of PSD estimation were recently discussed in great detail [30]. It is suggested that no single metric of the transfer matrix (e.g., column rank) can be used to predict the quality of the estimation. Instead, the stability of the inversion is related to the transfer matrix column rank, condition number, and signal-to-noise ratio (SNR). These three properties are related, as, for instance, the SNR is high and the matrix rank is low when weak gradients are applied.

As previously shown [29,30], a judicious choice of specific experimental parameters, and/or increased parametric space dimensionality (by adding more varying parameters, e.g., Δ, δ)

improves the stability of the size distribution estimation. For the purpose of introducing the current framework, a d-PFG 2-D parametric space was assumed, with linear steps in q and φ. Any experimental design optimization can be incorporated into the estimation framework, as a preliminary step.

Throughout the study the estimation quality was assessed based on the Jensen difference [37] between the theoretical and estimated PSDs. The Jensen difference metric is based on the Kullback–Leibler divergence, only it is symmetric and it always yields a finite value. The difference between two PSDs, Q and P, is defined as [38]

$$d_{JD} = \sum_i \left[\frac{P_i \ln(P_i) + Q_i \ln(Q_i)}{2} - \left(\frac{P_i + Q_i}{2} \right) \ln \left(\frac{P_i + Q_i}{2} \right) \right]. \tag{5}$$

The Jensen difference metric was chosen since it is a well-established method of measuring the similarity between two probability distributions. This comparison is made possible since all of the theoretical PSDs are known (either in the case of the phantom or simulations). In all cases, lower distance value reflects higher similarity, and thus higher quality of estimation.

4. Results

4.1. Resolving different PSDs

We first solve Eq. (4) to provide an estimate of the monodisperse PSD of each of the GCAs, i.e., two $R = 2.5$ μm blocks, two $R = 5$ μm arrays, and two $R = 13.7$ μm arrays. Six different ROIs were selected accordingly, and are marked by different letters and colors on a proton density MR image of the phantom (Fig. 3G). The corresponding PSD of each of the marked single-size ROIs is presented in Figs. 3A–F. Estimated values of the size distribution are indicated in red; the expected theoretical values are indicated in blue.

To fully exploit the PSD phantom and to further demonstrate the method's stability, three different ROIs were randomly selected (Fig. 4D). Each ROI included different volumetric fractions of all three nominal capillary radii. The ROIs are indicated by different letters and colors on a proton density MR image of the phantom (Fig. 4D). The corresponding PSD of each of the marked 3-size ROIs is presented in Figs. 4A–C. Estimated values of the size distribution are indicated in red; the theoretical values are indicated in blue. The Jensen difference between the theoretical and estimated PSDs from the different ROIs are detailed in Table 1.

Figs. 5A and B show experimental fits for two of the ROIs in Fig. 4D, ROI B and C, respectively. The signal attenuation shows a significant difference between the two cases, which reflects the variation in the PSD.

The PSD phantom consists of fused tubes, therefore there is no free water between them since that space is occupied by fused glass. Free water layers are present between the different glass wafers, and their fraction, f_G, is detected from the solution of Eq. (3). The careful water-filling procedure of the phantom leads to a very small free water volume between the wafers, and for all of the above ROIs, $f_G < 0.01$. A careful study of the effect of increasing the free water fraction is followed.

4.2. Free water fraction estimation

To establish that the presented method can reliably reconstruct a PSD while accurately estimating the free water fraction, water has to be present in significant quantities. The small free water fraction quantities within the phantom (see previous section) do not establish the reliability of the technique.

Free water was present in the upper part of the MRI phantom, which allowed the demonstration of the estimation of the free water fraction, f_G. This step was achieved by choosing a baseline PSD, which was a constant ROI that includes two different GCAs (labeled “ROI” in Fig. 6D). Then, three different free water volumes from the free water pool were added to the baseline ROI. These water volumes corresponded to the volumetric fractions, $f_G = 0.2, 0.27, 0.37$.

In addition to the radii and their relative fractions, the free water fractions were estimated in each case and are all presented in Figs. 6A–C. As before, the same color legend was used, namely, red and blue text and bins for estimated and theoretical, respectively.

4.3. s-PFG vs. d-PFG

Even though the advantages of a d-PFG over an s-PFG experiment were theoretically demonstrated by Benjamini et al. [29] and more recently by Katz and Nevo [30], an experimental work to support the claims was still absent. The current reliable GCA phantom can provide the means for this comparison.

The ROIs chosen for the s-PFG experiment were identical to the ones used in the d-PFG experiment (Fig. 4D). The estimated PSDs in this case are shown in Figs. 7A–C. These estimations should be compared to their d-PFG counterparts in Figs. 4A–C. The Jensen distances (as defined in the Methods section) between the estimated and theoretical PSDs for both the single- and double-PFG cases are summarized in Table 1.

4.4. Complex and realistic PSD simulations

Although being accurate and robust, the main disadvantage of any phantom, and specifically the current one, is the finite number of different compartment sizes it comprises. Reconstructing a continuous PSD would present a greater challenge, compared to a discrete one. Since such a phantom is not available, simulations can be used to test the framework under such conditions. For this purpose, two different continuous and complex PSDs (detailed in the Methods section) were generated.

The first PSD is a Bimodal-Gaussian function with overlapping wide peaks (with means 6.84, 11.99 μm and standard deviations 1.5, 2.0 μm). Two cases of SNR were analyzed with noise standard deviations of 0.5% and 1% relative to the signal attenuation without any diffusion gradient applied. In Fig. 8, the theoretical PSD was drawn as a function of the radius (solid line), and the estimated PSD was overlaid on it (bins). Figs. 8A and B correspond to noise standard deviations of 0.5% and 1%, and their Jensen differences were 0.0239 and 0.0435, respectively.

The second PSD is more complex, and is composed of two different functions, lognormal and Gaussian, and three peaks (with means 3.00, 11.65, 16.28 μm and standard deviations 4.0, 1.1, 1.2 μm). As before, the same two cases of SNR were tested. In Fig. 9, the theoretical PSD was drawn as a function of the radius (solid line), and the estimated PSD was overlaid on it (bins). Figs. 9A and B correspond to noise standard deviation of 0.5% and 1%, and their Jensen differences were 0.0200 and 0.0249, respectively.

5. Discussion

The spatially resolved PSD estimates obtained from the 2-D d-PFG MRI experiments agree with those derived based on light microscopy [26] (for compartment size) and proton density MRI intensity (for volumetric fraction). This study provides a vital step towards the migration of this method from NMR to MRI. Without a viable MRI phantom, imaging-related issues cannot be addressed, and validation of this framework is not possible. The main goal of this 2-D method is to provide comprehensive microstructural information with sub-voxel resolution. The GCA phantom is constructed from vertically stacked wafers with a known size distribution (Fig. 2), and therefore any image slice orientation would not lead to a PSD within a voxel. This inherent limitation led us to use ROI-based analysis, which bears the closest resemblance to a pixel-by-pixel estimate.

One major issue with MRI acquisition is the so-called “noise floor” [39]. This noise-induced bias in the magnitude signal, which is often absent in NMR acquisitions where SNR is generally larger than in MRI, is particularly significant at high diffusion-weighting and is also related to the compartment size. Without applying elaborate signal transformations to remove this bias [39], the gradient amplitude had to be restricted to a maximal value, above which the signal from the largest compartment in the porous structure reaches the noise floor.

Another aspect that is unique to MRI is the potential cross-terms between diffusion and imaging gradients. A short separation time (ST) between diffusion and imaging gradients might influence pore size estimation if the last diffusion gradient could not refocus the magnetization. The effect of using different values of ST was previously investigated [26] and resulted in very minor differences in the estimation. We have examined how incorporating imaging gradients in the signal calculation affects the transfer matrix and found that, even when using short ST, the effect is smaller than 0.1%. Nevertheless, we have included the slice selection gradients in the calculation in an attempt to reach the most accurate signal attenuation curves. It is worth noting that this effect is expected to increase under different experimental conditions, such as smaller slice thickness.

The underlying geometry of the different GCAs was first established, by selecting ROIs with single size pores and accurately estimating their size according to the known values (Fig. 3). The versatility and stability of the method was later demonstrated by randomly choosing three ROIs, which included different volumetric fractions of all three nominal capillary radii. All of the PSD estimations were reconstructed with high accuracy, as evident from Table 1.

The free water fraction in Eq. (3) was estimated throughout this study. Since there is no free water between the fused tubes in the GCA phantom, most of the signal from this phantom originates from restricted diffusion, therefore leading to a very small free water fraction. Larger free water fractions had to be investigated to establish the stability of the method by considering a bulk water volume that was present on the upper part of the phantom. As the result of an analysis of three different free water fractions in significant quantities, their fractions, along with their PSDs, were accurately estimated.

It has been recently shown [40] that an s-PFG experiment with a varying diffusion period is equivalent to a d-PFG experiment to the second moment of the total signal decay. While in some applications it may be wise to use such an s-PFG experiment and gain better SNR (due to higher signal intensity), for the PSD estimation problem a d-PFG experiment is still preferable. As previously shown [30], the application of two gradient pairs allows a better differentiation of different pores sizes, resulting in a higher transfer matrix rank. In addition, the experimental parameter space of a d-PFG sequence is inherently of a higher order, which can increase the inversion's stability [29].

The advantage of d-PFG over s-PFG in the context of the PSD estimation problem was experimentally shown in this study. The estimated PSDs resulting from the s-PFG experiment were quite far from the theoretical ones, as opposed to results from the d-PFG experiment (Table 1). The s-PFG experiment failed to accurately reconstruct the PSD even for the relatively simple and discrete size distribution of the GCA phantom. One of the reasons for this limitation is that an s-PFG experiment has only one experimental variable, G, where the d-PFG has two, G and φ. This simple yet important notion was studied and discussed in our previous publications. In addition to the extended information resulting from the 2-D acquisition, the s-PFG experiment has a lower number of maximal acquired data points, since the minimal increment of G is limited by the hardware. This property does not limit the d-PFG experiment, and therefore reconstructing complex PSDs with a large number of acquired data points could become feasible.

In the present study the pore size distribution phantom consists of discrete sizes. A more accurate representation of the pore size distribution found in natural samples would be a continuous one. As such a distribution is impossible to create artificially and in a controlled manner, a discrete distribution was used. From a mathematical standpoint, as the PSD vector includes a greater number of non-zero values in it, its reconstruction becomes less stable and less accurate. Simulations of two different and representative continuous PSDs were used to account for this gap in experimental ability. These continuous PSDs were generated to account for important properties that are absent in the GCA phantom, namely, large standard deviations, overlapping peaks, and a variety of functional shapes. For each of the simulated PSDs, two noise levels were analyzed ($\sigma = 0.005, 0.01$). As known for ill-conditioned problems, the presence of noise reduces the accuracy of the reconstruction, and indeed the quality of the estimation in all the simulations is lower as noise level is higher (indicated by the Jensen differences). Nevertheless, even for the highest noise level, the estimated PSDs were in good agreement with the theory.

The underlying assumptions of the method concern the axons geometry and orientation, as they are assumed to be coherent infinite cylinders. The current 2-D circular gradient sampling scheme was chosen because of the ideal nature of the phantom, namely, the cylinders are aligned orthogonal to the applied gradient pulses. Although this modeling approach has been widely used to date [33,41,27,36], it would introduce a systematic error to the analysis of brain white matter tissue, where the fibers take on all possible orientations across an image. In this case, a 3-D d-PFG acquisition scheme could be used, as proposed and applied by Komlosh et al. [5]. A 3-D gradient sampling scheme involves the application of the circular acquisition in different orientations, as used in Diffusion Tensor Imaging. The principal fiber orientation in each voxel can then be calculated from a subset of the measurements, and the projection of the data onto the perpendicular plane is used and analyzed. Although it increases the experimental time, a 3-D sampling scheme is essential when dealing with complex white matter (as opposed to spinal cord).

The relatively long acquisition time (7 h) is not acceptable for clinical applications. A significant reduction in acquisition time can be achieved by a judicious choice of specific experimental parameters from the infinite possible different sets. Employing such an optimization scheme [29,30] may lower the number of acquisitions while improving the size distribution reconstruction.

An important aspect of this study is that the derived PSD is nonparametric, so it is not based on any assumption regarding its shape. Moreover, it is robust to variation in initial conditions. In neuronal tissue, while a parametric PSD may accurately describe healthy, normal tissue, a nonparametric PSD provides an objective description of any white matter tissue, regardless of its viability, pathological state, or stage in development.

6. Conclusions

This work demonstrates the feasibility of a spatially resolved PSD estimation using a d-PFG based method on a phantom that is specifically suitable to simulate axonal geometry. Other heterogeneous biological samples such as skeletal muscle and spinal cord will be investigated in the near future. The complex microstructural architecture of these tissues would be suitable for the same voxel-based analysis, and the information obtained from the compartment-size distribution would shed light on their normal or abnormal development and function. Obtaining spatiality resolved PSD would also be useful for non-biological materials, such as drug-eluting porous biomaterials. This method will allow *in vivo* structural changes of such implanted biomaterial devices to be followed, and for their continuous microstructural transformation to be reported over time.

Acknowledgments

This work was supported by funds provided by the Intramural Research Program of the *Eunice Kennedy Shriver* National Institute of Child Health and Human Development (NICHD), and the Center for Neuroregenerative Medicine (CNRM) under the auspices of the Henry Jackson Foundation (HJF). The authors would like to thank Liz Salak for editing the manuscript.

References

1. Elsner JJ, Zilberman M. Antibiotic-eluting bioresorbable composite fibers for wound healing applications: microstructure, drug delivery and mechanical properties. Acta Biomater. 2009; 5(8):2872–2883. [PubMed: 19416766]
2. Hollingsworth K, Johns M. Measurement of emulsion droplet sizes using PFG NMR and regularization methods. J. Colloid Interface Sci. 2003; 258(2):383–389. [PubMed: 12618109]
3. Callaghan P, Jolley K, Humphrey R. Diffusion of fat and water in cheese as studied by pulsed field gradient nuclear magnetic resonance. J. Colloid Interface Sci. 1983; 93(2):521–529.
4. Song Y, Ryu S, Sen P. Determining multiple length scales in rocks. Nature. 2000; 406(6792):178–181. [PubMed: 10910355]
5. Komlosh ME, Özarslan E, Lizak MJ, Horkayne-Szakaly I, Freidlin RZ, Horkay F, Basser PJ. Mapping average axon diameters in porcine spinal cord white matter and rat corpus callosum using d-PFG MRI. NeuroImage. 2013; 78:210–216. [PubMed: 23583426]
6. Tasaki I, Ishii K, Ito H. On the relation between the conduction-rate, the fiber-diameter and the internodal distance of the medullated nerve fiber. Jpn. J. Med. Sci. III, Biophys. 1943; 9:189–199.
7. Waxman, S, Kocsis, J, Stys, P. The Axon: Structure, Function, and Pathophysiology. New York: Oxford University Press; 1995.
8. Cluskey S, Ramsden DB. Mechanisms of neurodegeneration in amyotrophic lateral sclerosis. Molec. Pathol. 2001; 54(6):386–392. [PubMed: 11724913]
9. Trapp BD, Peterson J, Ransohoff RM, Rudick R, Mörk S, Bö L. Axonal transection in the lesions of multiple sclerosis. New England J. Med. 1998; 338(5):278–285. [PubMed: 9445407]
10. Stejskal E, Tanner J. Spin diffusion measurements: spin echoes in the presence of a time-dependent field gradient. J. Chem. Phys. 1965; 42(1):288–292.
11. Callaghan, P. Principles of Nuclear Magnetic Resonance Microscopy. New York: Oxford University Press; 1991.
12. Topgaard D, Malmborg C, Söderman O. Restricted self-diffusion of water in a highly concentrated w/o emulsion studied using modulated gradient spinecho NMR. J. Magnet. Reson. 2002; 156(2):195–201.
13. Kuchel PW, Coy A, Stilbs P. NMR diffusion-diffraction of water revealing alignment of erythrocytes in a magnetic field and their dimensions and membrane transport characteristics. Magn. Reson. Med. 1997; 37(5):637–643. [PubMed: 9126936]
14. Callaghan P, Coy A, MacGowan D, Packer K, Zelaya F. Diffraction-like effects in NMR diffusion studies of fluids in porous solids. Nature. 1991; 351:467–469.
15. Laun FB, Kuder TA, Semmler W, Stieltjes B. Determination of the defining boundary in nuclear magnetic resonance diffusion experiments. Phys. Rev. Lett. 2011; 107(4):048102. [PubMed: 21867047]
16. Basser PJ. Relationships between diffusion tensor and q-space MRI. Magn. Reson. Med. 2002; 47(2):392–397. [PubMed: 11810685]
17. Malmberg P, Nygren H. A method for evaluating the influence of porosity on the early reactions of blood with materials. Biomaterials. 2002; 23(1):247–253. [PubMed: 11762844]
18. Dunne NJ, Orr JF, Mushipe MT, Eveleigh RJ. The relationship between porosity and fatigue characteristics of bone cements. Biomaterials. 2003; 24(2):239–245. [PubMed: 12419624]
19. Cory D, Garroway A, Miller J. Applications of spin transport as a probe of local geometry. Polym. Preprints. 1990; 31:149–150.
20. Mitra P. Multiple wave-vector extensions of the NMR pulsed-field-gradient spin-echo diffusion measurement. Phys. Rev. B. 1995; 51(21):15074–15078.
21. Lawrenz M, Finsterbusch J. Detection of microscopic diffusion anisotropy on a whole-body MR system with double wave vector imaging. Magn. Reson. Med. 2011; 66(5):1405–1415. [PubMed: 21488098]
22. Ozarslan E. Compartment shape anisotropy (CSA) revealed by double pulsed field gradient MR. J. Magn. Reson. 2009; 199(1):56–67. [PubMed: 19398210]

23. Shemesh N, Özarslan E, Basser PJ, Cohen Y. Accurate noninvasive measurement of cell size and compartment shape anisotropy in yeast cells using double-pulsed field gradient MR. NMR Biomed. 2012; 25(2):236–246. [PubMed: 21786354]

24. Koch MA, Finsterbusch J. Compartment size estimation with double wave vector diffusion-weighted imaging. Magn. Reson. Med. 2008; 60(1):90–101. [PubMed: 18421690]

25. Shemesh N, Ozarslan E, Basser PJ, Cohen Y. Detecting diffusion-diffraction patterns in size distribution phantoms using double-pulsed field gradient NMR: theory and experiments. J. Chem. Phys. 2010; 132(3):034703. [PubMed: 20095748]

26. Komlosh ME, Özarslan E, Lizak MJ, Horkay F, Schram V, Shemesh N, Cohen Y, Basser PJ. Pore diameter mapping using double pulsed-field gradient MRI and its validation using a novel glass capillary array phantom. J. Magn. Reson. 2011; 208(1):128–135. [PubMed: 21084204]

27. Assaf Y, Blumenfeld-Katzir T, Yovel Y, Basser PJ. AxCaliber: a method for measuring axon diameter distribution from diffusion MRI. Magn. Reson. Med. 2008; 59(6):1347–1354. [PubMed: 18506799]

28. Farrar DE, Glauber RR. Multicollinearity in regression analysis: the problem revisited. Rev. Econom. Stat. 1967; 49(1):92–107.

29. Benjamini D, Katz Y, Nevo U. A proposed 2D framework for estimation of pore size distribution by double pulsed field gradient NMR. J. Chem. Phys. 2012; 137(22):224201. [PubMed: 23248996]

30. Katz Y, Nevo U. Quantification of pore size distribution using diffusion NMR: experimental design and physical insights. J. Chem. Phys. 2014; 140(16):164201. [PubMed: 24784263]

31. Benjamini D, Nevo U. Estimation of pore size distribution using concentric double pulsed-field gradient NMR. J. Magn. Reson. 2013; 230:198–204. [PubMed: 23548563]

32. Benjamini D, Elsner JJ, Zilberman M, Nevo U. Pore size distribution of bioresorbable films using a 3-D diffusion NMR method. Acta Biomater. 2014; 10(6):2762–2768. [PubMed: 24534719]

33. Assaf Y, Freidlin RZ, Rohde GK, Basser PJ. New modeling and experimental framework to characterize hindered and restricted water diffusion in brain white matter. Magn. Reson. Med. 2004; 52(5):965–978. [PubMed: 15508168]

34. Packer K, Rees C. Pulsed NMR studies of restricted diffusion: I. Droplet size distributions in emulsions. J. Colloid Interface Sci. 1972; 40(2):206–218.

35. Grebenkov DS. Laplacian eigenfunctions in NMR: I. A numerical tool. Concepts Magn. Reson. Part A. 2008; 32A(4):277–301.

36. Ozarslan E, Shemesh N, Basser PJ. A general framework to quantify the effect of restricted diffusion on the NMR signal with applications to double pulsed field gradient NMR experiments. J. Chem. Phys. 2009; 130(10):104702. [PubMed: 19292544]

37. Endres D, Schindelin J. A new metric for probability distributions. IEEE Trans. Inform. Theory. 2003; 49(7):1858–1860.

38. Sibson R. Information radius. Zeitschrift Wahrscheinlichkeitstheorie Verwandte Gebiete. 1969; 14(2):149–160.

39. Koay CG, Özarslan E, Basser PJ. A signal transformational framework for breaking the noise floor and its applications in MRI. J. Magn. Reson. 2009; 197(2):108–119. [PubMed: 19138540]

40. Jespersen SN. Equivalence of double and single wave vector diffusion contrast at low diffusion weighting. NMR Biomed. 2012; 25(6):813–818. [PubMed: 22134913]

41. Ozarslan E, Basser PJ. MR diffusion – “diffraction” phenomenon in multipulse-field-gradient experiments. J. Magn. Reson. 2007; 188(2):285–294. [PubMed: 17723314]

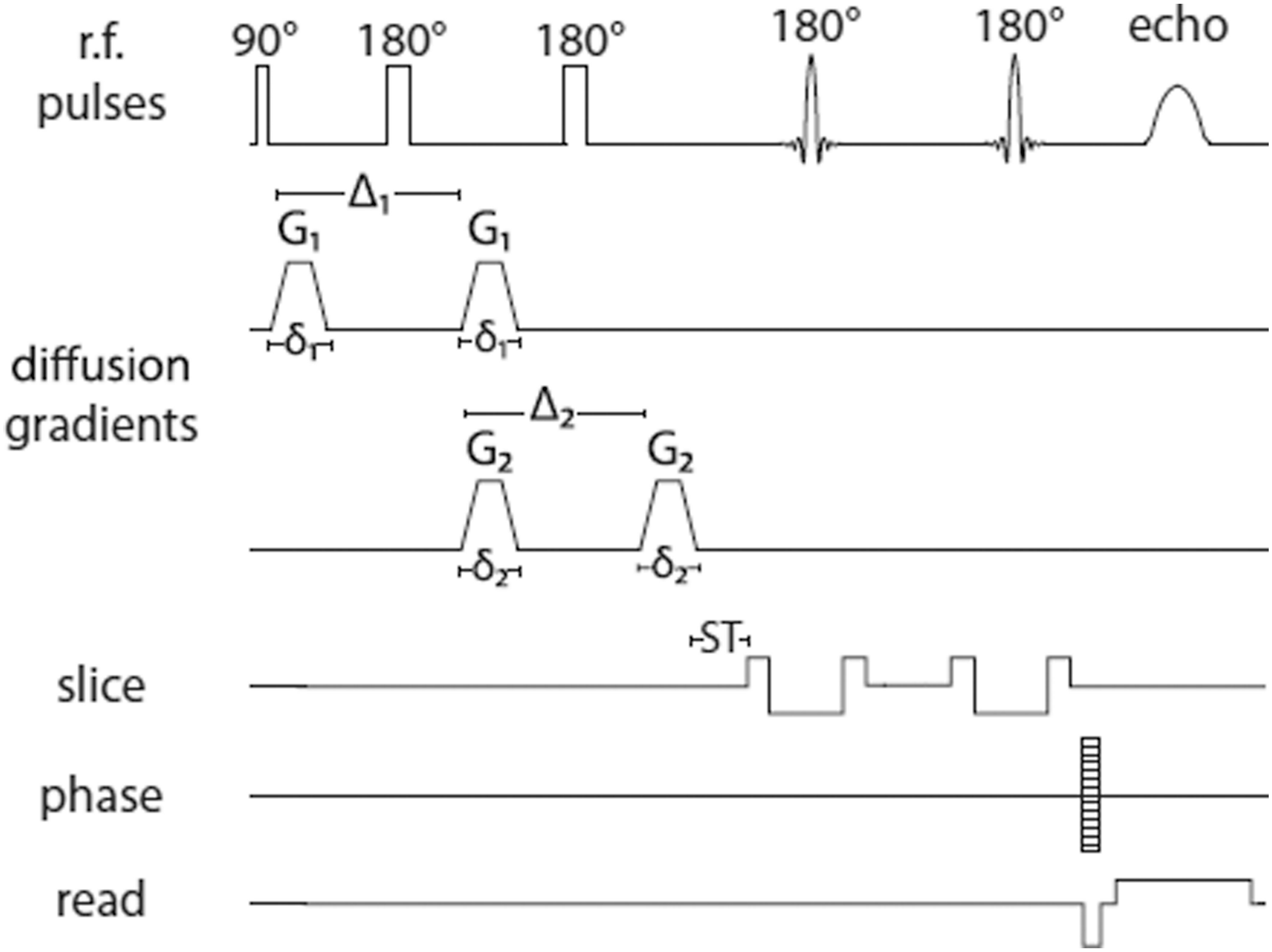

Fig. 1.

The d-PFG filtered MRI pulse sequence used in this study.

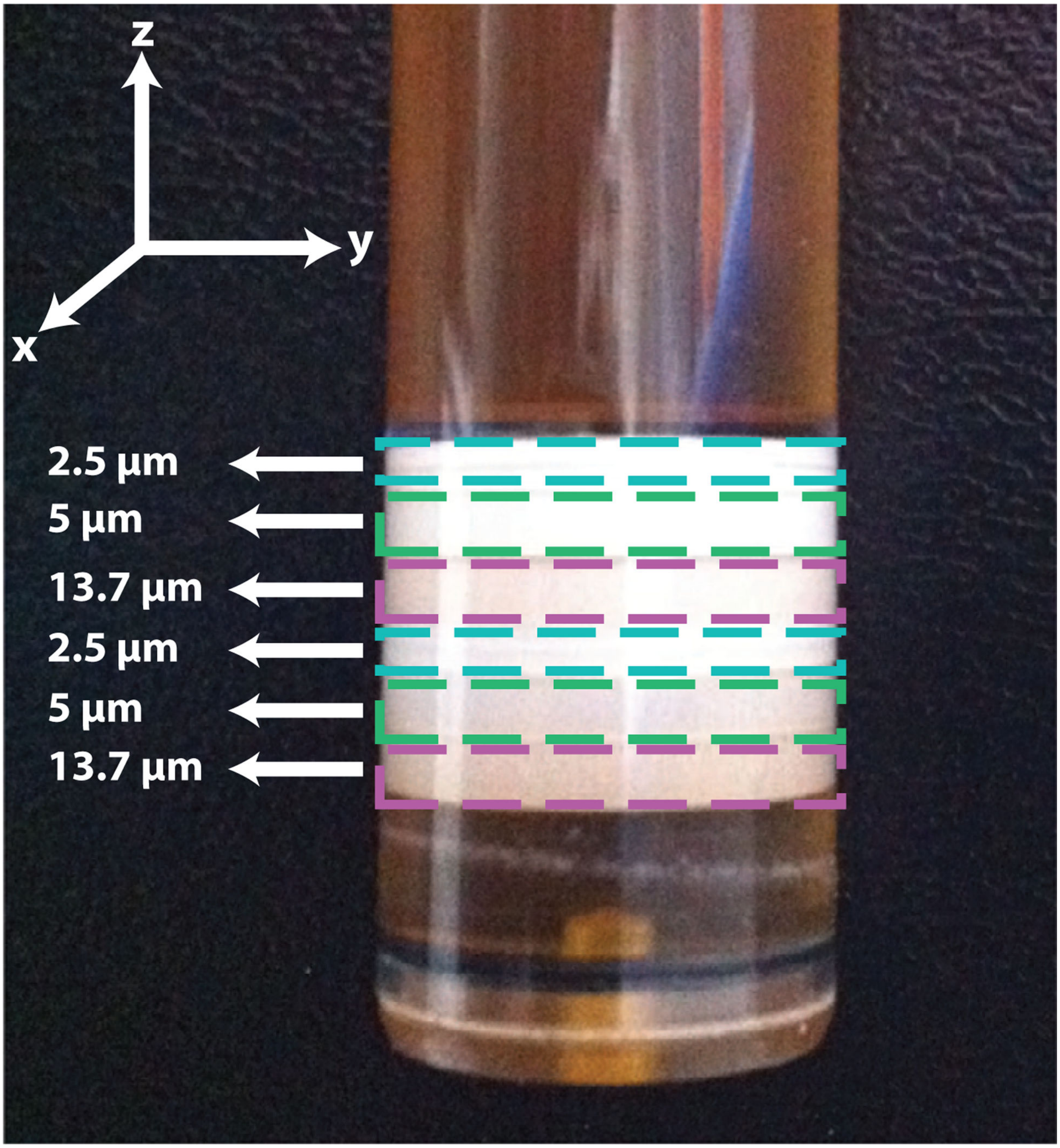

Fig. 2.

A photo of the GCA PSD phantom placed in the NMR tube. Each GCA and its size is indicated.

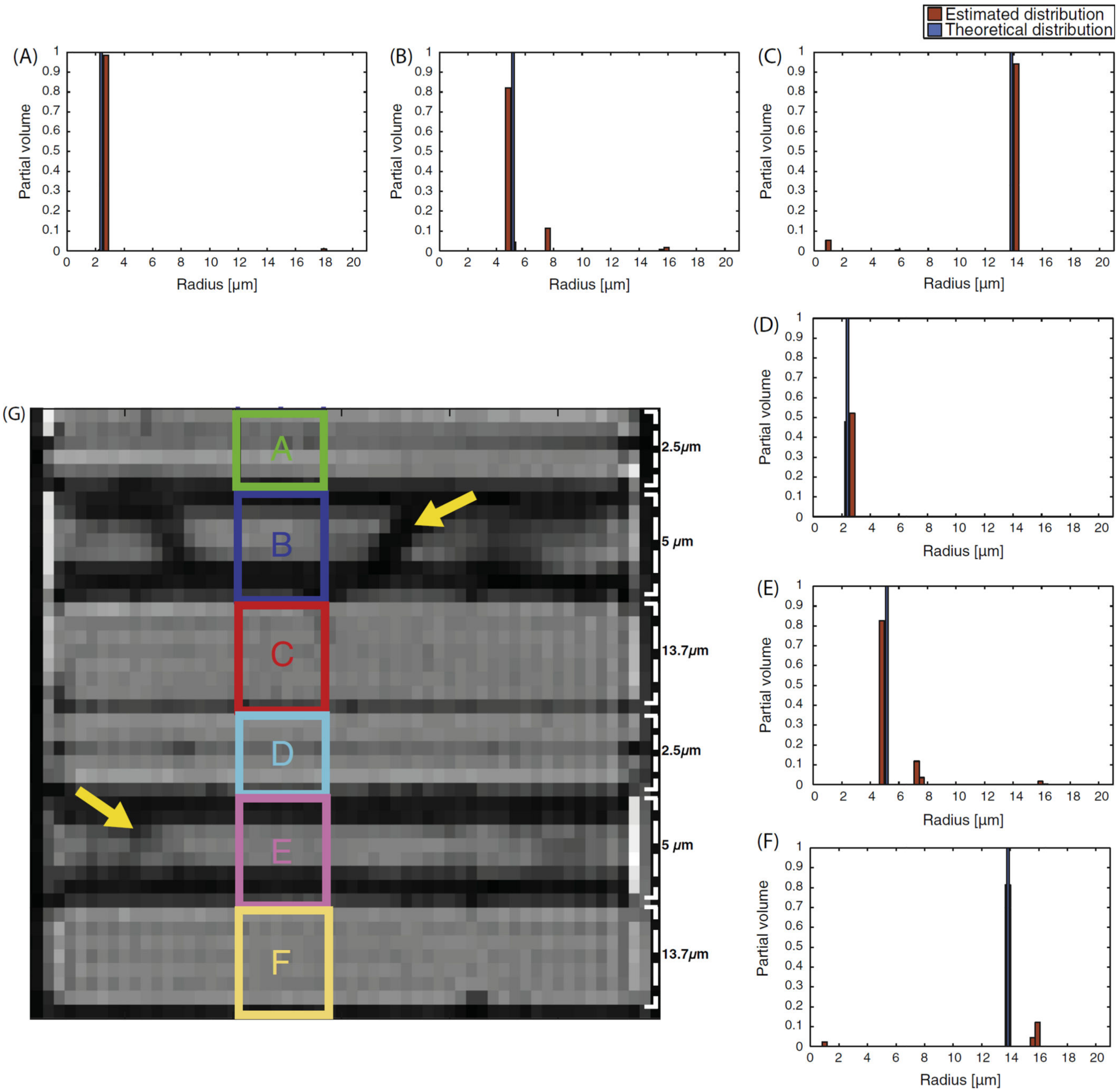

Fig. 3.

A separate ROI-based estimation of the PSD of each of the 6 GCAs. The ROI of each of the PSDs (A–F) is marked on a proton density image (G), where some imperfections in the GCA are indicated by a yellow arrow. Estimated values of the size distribution are indicated in red, while the expected theoretical values are indicated in blue. (For interpretation of the references to colour in this figure legend, the reader is referred to the web version of this article.)

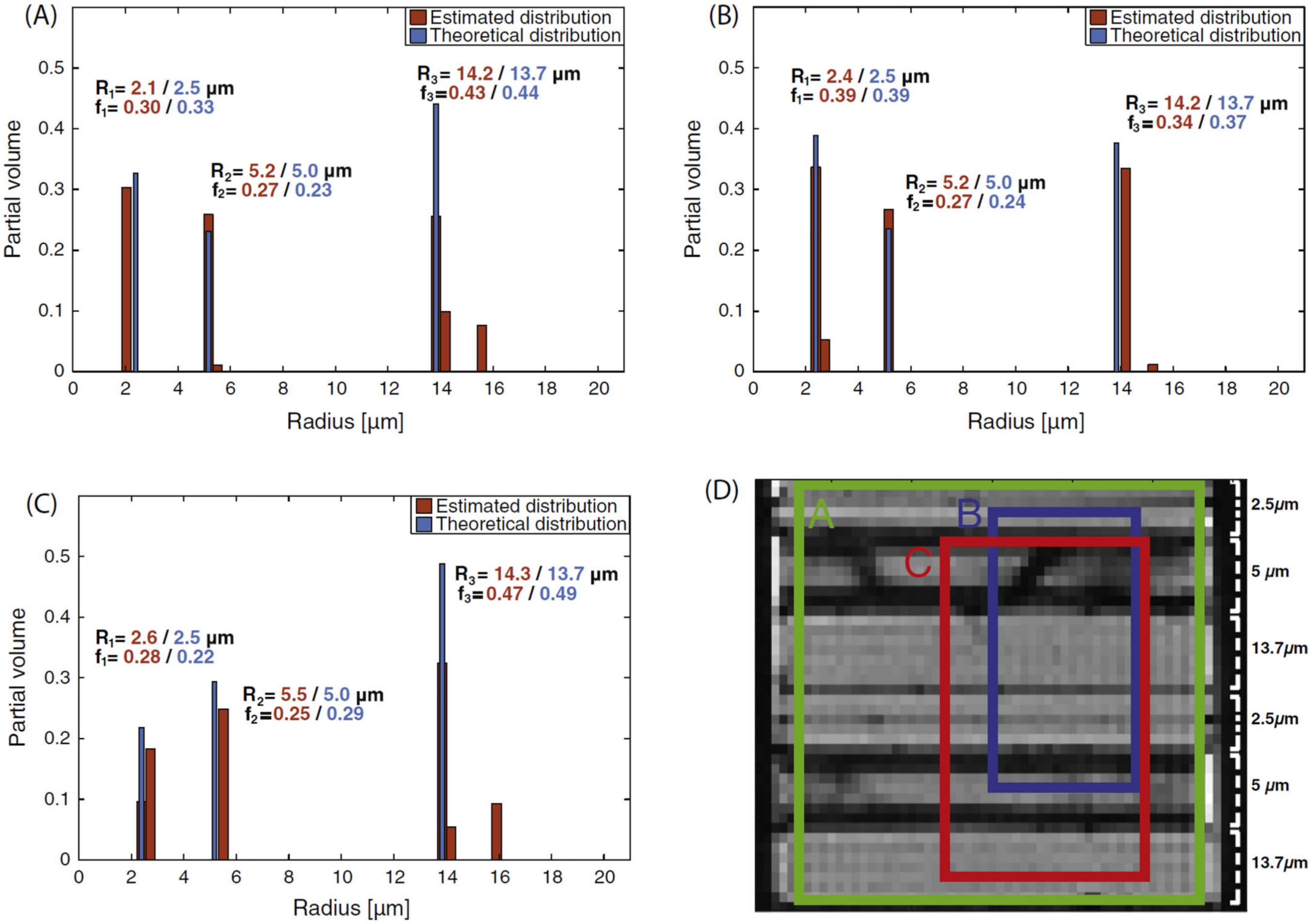

Fig. 4.

Overlapped on a proton density image (D) are three ROIs that include different volumetric fractions of all three nominal capillary radii, indicated by *A, B, C*, and their estimated PSDs in (A), (B), and (C), respectively. The ROIs were randomly chosen to include different combinations of three GCAs. Estimated values of the size distribution are indicated in red; theoretical values are indicated in blue. (For interpretation of the references to colour in this figure legend, the reader is referred to the web version of this article.)

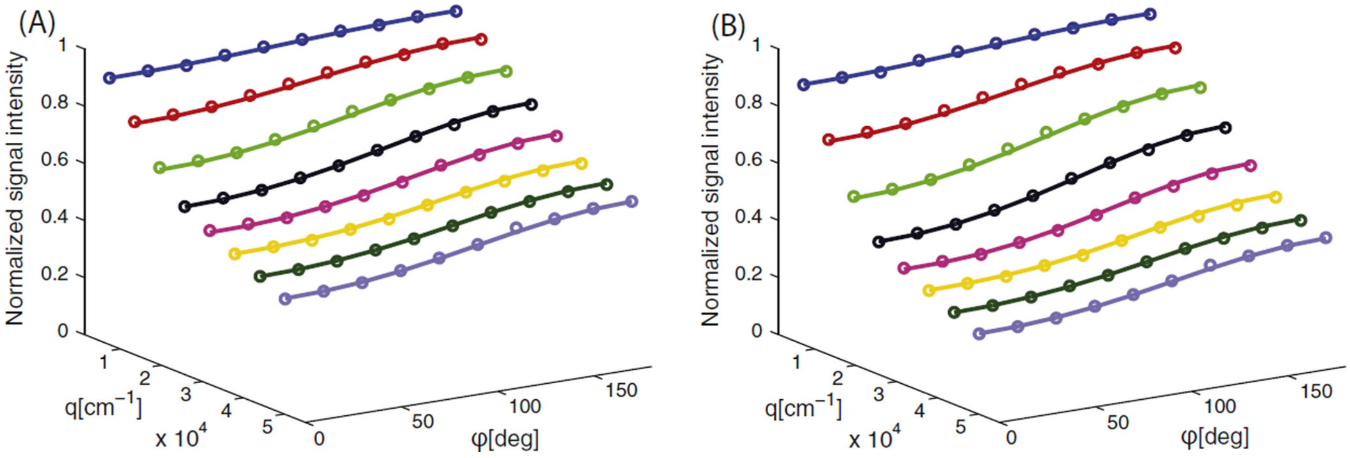

Fig. 5.

Experimental data (symbols) and their estimated values (solid line) for two of the ROIs in Fig. 4. (A) corresponds to Fig. 4B, and (B) corresponds to Fig. 4C. Different colors indicate angular dependency with different q-values. (For interpretation of the references to colour in this figure legend, the reader is referred to the web version of this article.)

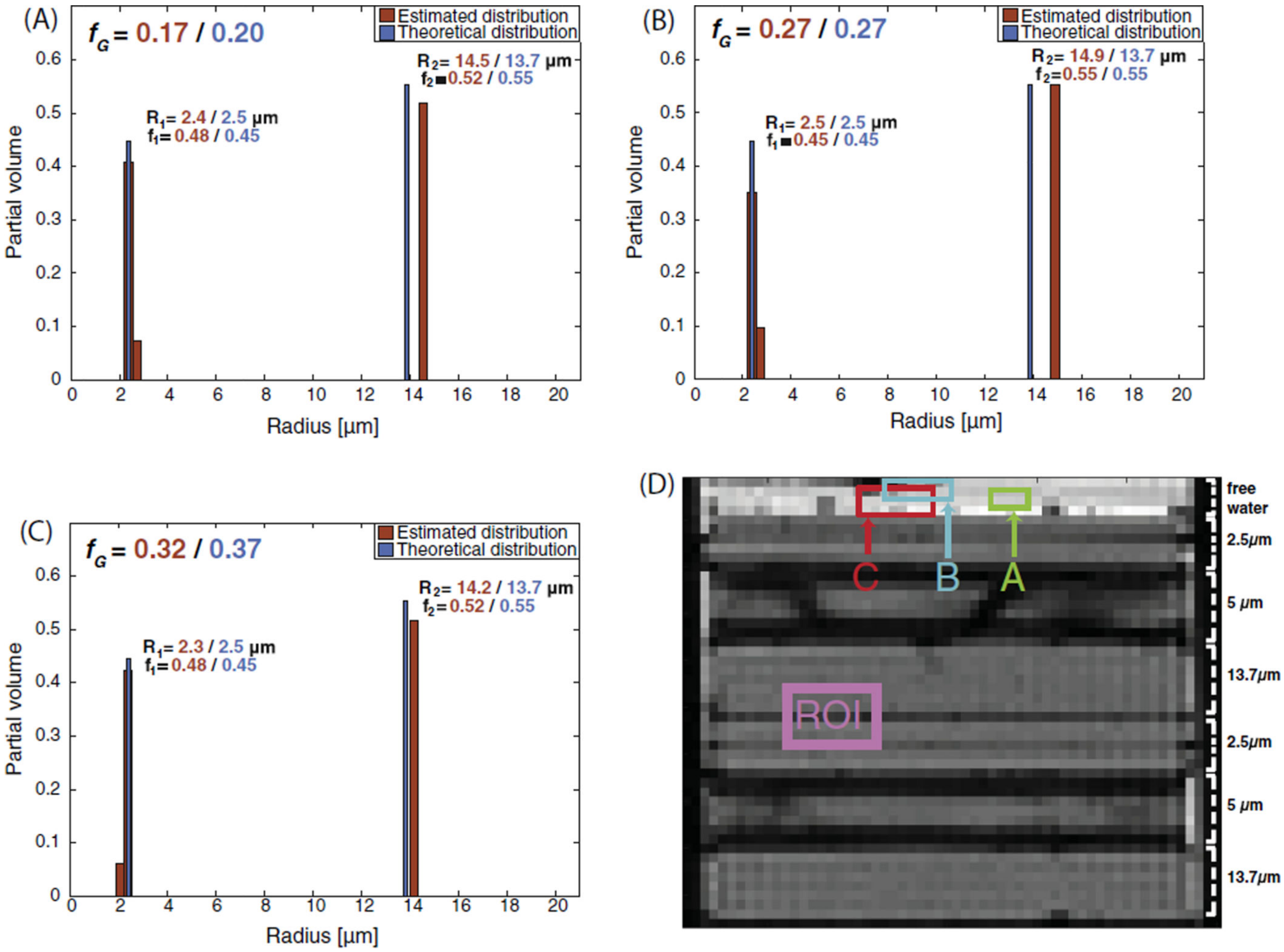

Fig. 6.

A constant ROI along with three free water volumes are indicated on a proton density image (D). The estimated PSDs with different free water fractions are shown in (A), (B), and (C). Estimated values of the size distribution are indicated in red, while the expected theoretical values are indicated in blue. (For interpretation of the references to colour in this figure legend, the reader is referred to the web version of this article.)

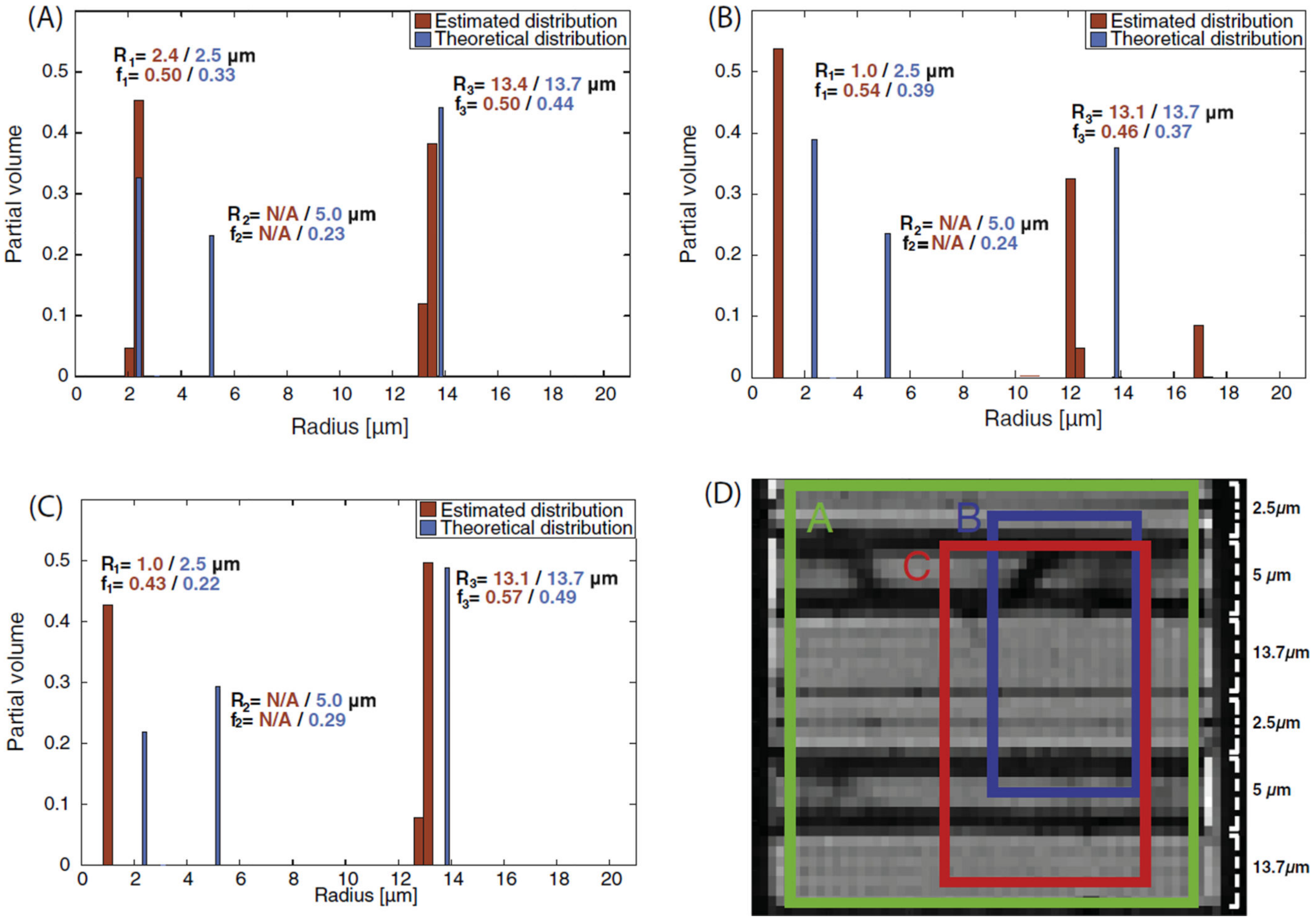

Fig. 7.

Overlapped on a proton density image (D) are the same three ROIs that were used in the d-PFG case (Fig. 4D) and their estimated PSDs from the s-PFG experiment in (A), (B), and (C), respectively. Estimated values of the size distribution are indicated in red; the theoretical values are indicated in blue. (For interpretation of the references to colour in this figure legend, the reader is referred to the web version of this article.)

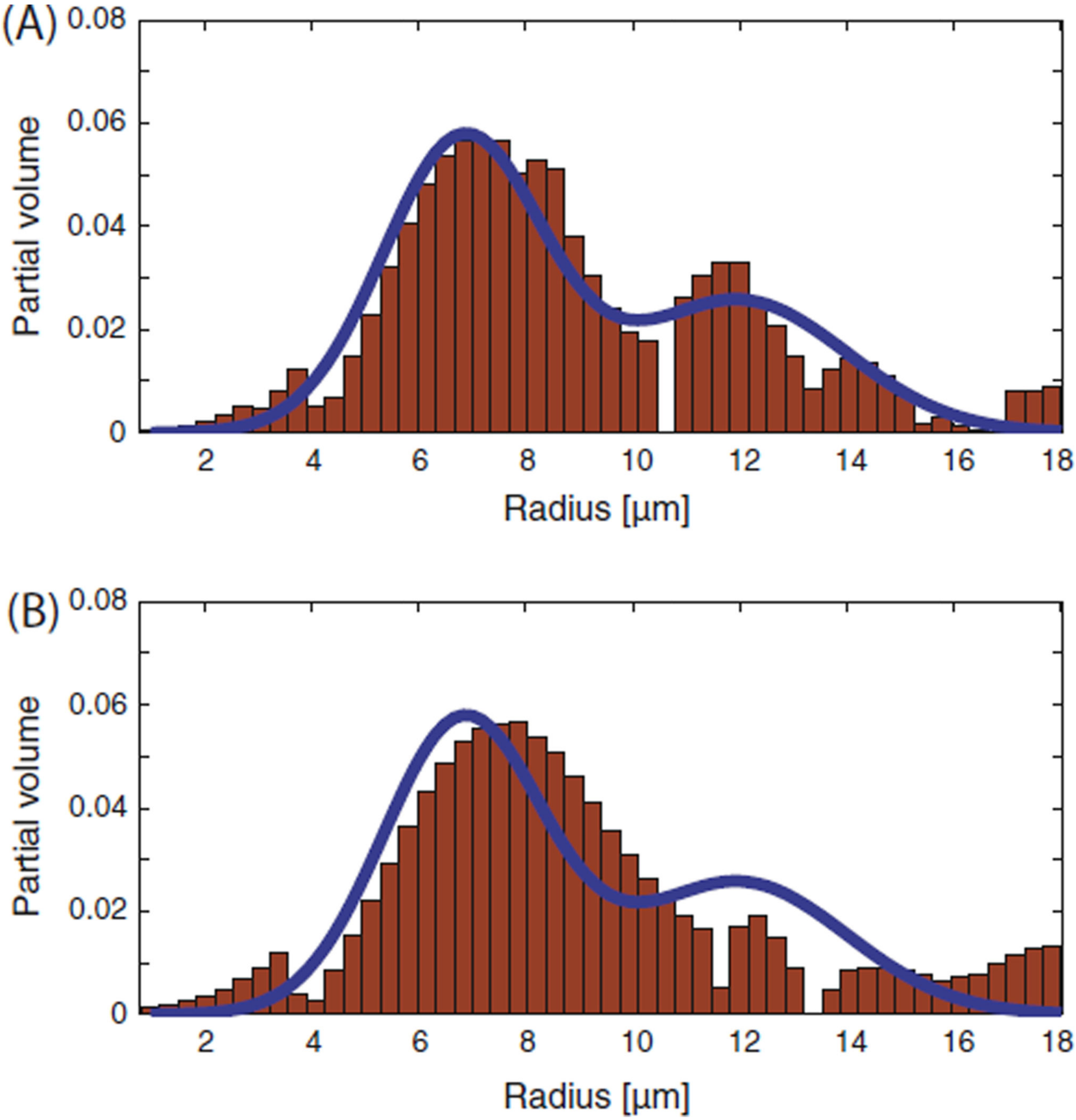

Fig. 8.

PSD estimation (bins) of a simulated Bimodal-Gaussian function (solid line) with overlapping wide peaks. Two noise standard deviations of (A) 0.5% and (B) 1% relative to the signal attenuation without any diffusion gradient applied, were used.

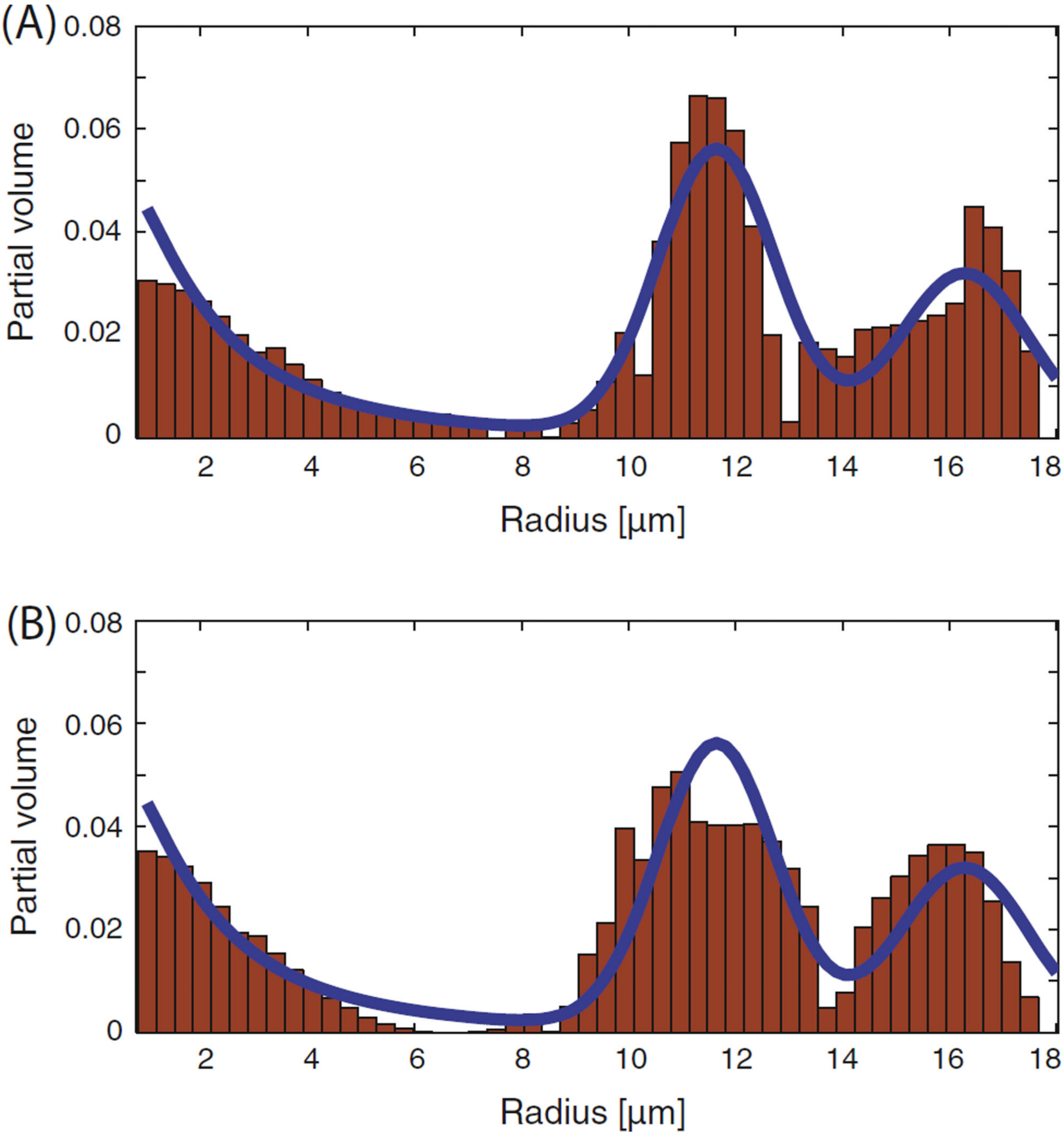

Fig. 9.

A PSD composed of lognormal and Gaussian functions (solid line) and its estimation (bins). Two noise standard deviations of (A) 0.5% and (B) 1% relative to the signal attenuation without any diffusion gradient applied, were used.

Table 1

Jensen difference between the estimated and theoretical PSDs for both single- and double-PFG experiments.

ROI	**A**	**B**	**C**
d-PFG	0.2951	0.2697	0.3224
s-PFG	0.4275	0.6931	0.6931